On the problem of a Gurtin-Murdoch cylindrical material surface embedded in an infinite matrix

Zhilin Han^{a,b}, Sofia G. Mogilevskaya^{c,*}, Anna Y. Zemlyanova^d

^aShanghai High Performance Fibers and Composites Center (Province-Ministry Joint), Center for Civil Aviation Composites, Donghua University, Shanghai, China, 201620 ^bCollege of Science, Donghua University, Shanghai, China, 201620 ^cDepartment of Civil, Environmental, and Geo- Engineering, University of Minnesota, 500 Pillsbury Drive S.E., Minneapolis, MN, 55455, USA

^dDepartment of Mathematics, Kansas State University, 138 Cardwell Hall, Manhattan, Kansas, 66506, USA

Abstract

The problem of an infinite isotropic elastic matrix subjected to uniform far-field load and containing a Gurtin-Murdoch material surface of cylindrical shape is considered in plane strain setting. The governing equations and the boundary conditions for the problem, reduced to that of an infinite plane containing a material curve along a circular arc, are reviewed. The displacements inside the matrix are sought in the complex variables form of a single layer elastic potential whose density represents the jump in complex tractions across the curve. Exact complex integral representations for the elastic fields everywhere in the material are provided and the problem is further reduced to the system of real variables hypersingular boundary integral equations in terms of the strain and rotation components associated with the curve. The components are then approximated by the series of trigonometric functions that are multiplied by the square root weight functions to allow for automatic incorporation of the tip conditions. The unknown coefficients in the series are found from the system of linear algebraic equations that is solved using standard collocation method. The numerical examples are presented to illustrate the influence of dimensionless parameters with the main focus on the study of curvature-induced effects.

Keywords: Composites with ultra thin and stiff reinforcements, Gurtin-Murdoch theory,

1. Introduction

In this paper, we consider the plane strain problem of an infinite isotropic elastic matrix that contains a Gurtin-Murdoch material surface of cylindrical shape and subjected to uniform far-field load. The surface represents a membrane of vanishing thickness that is characterized by its own elastic stiffness and the residual surface tension. The possible applications of the problem are in the area of modeling composite materials that use ultra-thin stiff membranes as reinforcements, e.g., Cao (2014), Güler and Bağcı (2020), Papageorgiou et al. (2017, 2020), Suk et al. (2010), in particular, thick graphene reinforced composite cylindrical panels, e.g. Mirzaei and Abbasi (2023).

The idea that the existing material surface theories, Gurtin and Murdoch (1975, 1978), Steigmann and Ogden (1997, 1999), could be useful for modeling materials with flexible and extensible or inextensible reinforcements was suggested in several recent publications, see e.g. Baranova et al. (2020), Mogilevskaya et al. (2021b), Zemlyanova et al. (2023). However, the numerical solutions were reported there only for the case of a material surface along a straight segment.

Here, we present the numerical algorithm for solving the two-dimensional plane-strain problem involving a Gurtin-Murdoch curve along a circular arc and use it to investigate the influence of the curvature-related effects. As in Mogilevskaya et al. (2021b), Zemlyanova et al. (2023), we use the theories of elastic layer potentials and integral equations in order to present exact expressions for the elastic fields everywhere in the material. The problem is further reduced to the solution of the system of coupled real variables hypersingular boundary integral equations written in terms of the strain and rotation components associated

^{*}Corresponding author

Email addresses: hanzhilin@dhu.edu.cn (Zhilin Han), mogil003@umn.edu (Sofia G. Mogilevskaya), azem@ksu.edu (Anna Y. Zemlyanova)

with the arc. Using the approximations for the components that include the truncated series of trigonometric functions multiplied by the square root weight functions and employing standard collocation, we obtain the system of linear algebraic equations for the unknown series coefficients. The elastic fields in the matrix are then found using appropriate complex integral representations. The obtained solution is used to illustrate the influence of governing dimensionless parameters with the main focus on the curvature-induced effects. Additionally, we demonstrate that, unlike in the case of a material surface along a straight segment, the problem under study is not reducible to the problem of a rigid circular arc, solved in Liu and Jiang (1994).

The paper is structured as follows. In Section 2, we formulate the problem under study and review its governing equations. In Section 3, we introduce the complex variables representations for the geometry and fields involved, list the exact complex variables integral representations for the fields, and present the governing complex variable boundary integral equation. In Section 4, we reduce the latter equation to the system of real variables boundary integral equations and, after introducing the dimensionless parameters, reformulate the system in dimensionless settings. In Section 5, we describe major steps of the proposed numerical algorithm. In Section 6, we demonstrate that, unlike in the case of a material surface along a straight segment, the problem under study is not reducible to the problem of a rigid circular arc. Section 7 contains several examples of numerical simulations. Concluding remarks are presented in Section 8.

2. Problem formulation and governing equations

Consider the plane strain problem of an infinite isotropic elastic matrix that contains a Gurtin-Murdoch material curve located along the circular arc L of radius R with the tips at the points $\boldsymbol{\xi} = \mathbf{a}$, $\boldsymbol{\xi} = \mathbf{b}$, see Fig. 1. The matrix, characterized by the shear modulus μ and Poisson's ratio ν , is subjected to the uniform far-field load σ_{11}^{∞} , σ_{22}^{∞} , σ_{12}^{∞} . The origin

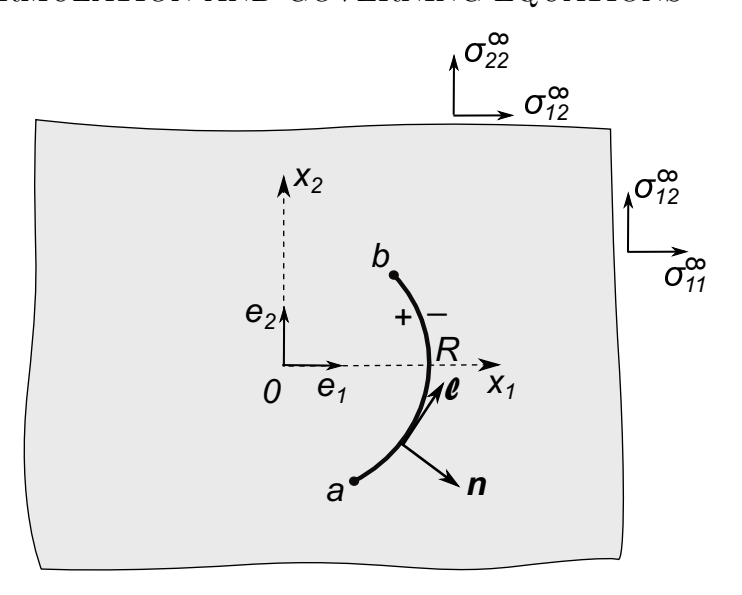


Figure 1: Problem configuration: a Gurtin-Murdoch circular material curve in an elastic matrix.

of the global Cartesian coordinate system with the unit basis vectors \mathbf{e}_1 , \mathbf{e}_2 is chosen to be located at the center of the arc. Additionally, the local coordinate system with the mutually orthogonal unit vectors \boldsymbol{n} , $\boldsymbol{\ell}$ is introduced and shown on Fig. 1.

According to the Gurtin-Murdoch theory, it is assumed that L is characterized by its own elastic stiffness parameters μ_S , λ_S and by the residual surface tension σ_0 . The governing equations for the theory include the standard Navier equation for the displacements inside the matrix supplemented by the conditions across L and at its tips. The supplemental conditions for the problem under study can be deduced from the corresponding conditions for a curve of an arbitrary sufficiently smooth shape reported in Mogilevskaya et al. (2021b), Zemlyanova et al. (2023), see also a review in Mogilevskaya et al. (2021a), by assuming that the local radius of curvature R = R(s) on L is constant.

Thus, the conditions for the fields across L at the point $\boldsymbol{\xi} \in L$ are (here and below we omitted the argument $\boldsymbol{\xi}$ for brevity)

$$u_1^+ = u_1^- = u_1, \ u_2^+ = u_2^- = u_2,$$
 (1)

3 REPRESENTATION OF THE GEOMETRY AND FIELDS BY COMPLEX VARIABLES5

$$\Delta \sigma_n = \sigma_n^+ - \sigma_n^- = -\frac{\sigma^S}{R} + \sigma_0 \frac{\partial \omega^S}{\partial s},\tag{2}$$

$$\Delta \sigma_{\ell} = \sigma_{\ell}^{+} - \sigma_{\ell}^{-} = \frac{\partial \sigma^{S}}{\partial s} + \sigma_{0} \frac{\omega^{S}}{R}, \tag{3}$$

where u_1 and u_2 are the displacement components of the bulk material in the global coordinate system, σ_n and σ_ℓ are the corresponding normal and shear tractions, and s is the arc length. The superscripts "+", "-" here and below describe the limit values of the fields when L is approached from the direction of that of the normal vector or from the opposite direction, respectively. The expressions for the surface stress σ^S , surface strain ε^S , and surface rotation ω^S involved in Eqs. (2)-(3) are

$$\sigma^S = \sigma_0 + (\lambda_S + 2\mu_S)\varepsilon^S,\tag{4}$$

$$\varepsilon^S = \frac{u_n}{R} + \frac{\partial u_\ell}{\partial s},\tag{5}$$

$$\omega^S = -\frac{u_\ell}{R} + \frac{\partial u_n}{\partial s},\tag{6}$$

in which u_n and u_ℓ are the normal and shear components of the displacements.

The conditions at the tips $\xi = \mathbf{a}$ and $\xi = \mathbf{b}$ of L are given by the following equations:

$$\sigma^S = 0, \ \sigma_0 \omega^S = 0. \tag{7}$$

3. Representation of the geometry and fields by complex variables

3.1. Complex variables combinations

We assume that the coordinates of the point $\xi \in L$ are combined in the complex variable $\tau = \tau_1 + i\tau_2$. The equation of the arc then can be expressed in complex variables as

$$\tau \bar{\tau} = R^2, \tag{8}$$

3 REPRESENTATION OF THE GEOMETRY AND FIELDS BY COMPLEX VARIABLES6 where a bar over a symbol denotes complex conjugation.

As in Mogilevskaya et al. (2021a,b), Zemlyanova et al. (2023), we introduce the complex variables displacements and tractions as

$$u = u_1 + iu_2, \ \sigma = \sigma_n + i\sigma_\ell, \tag{9}$$

where $i^2 = -1$.

Using the following transformation formulae, see e.g., Mogilevskaya et al. (2021a):

$$u_n + iu_\ell = iu \exp\left(-i\alpha\right),\tag{10}$$

$$\frac{\mathrm{d}}{\mathrm{d}s} = \exp\left(\mathrm{i}\alpha\right) \frac{\mathrm{d}}{\mathrm{d}\tau},\tag{11}$$

$$\frac{\mathrm{d}\alpha}{\mathrm{d}s} = \frac{1}{R},\tag{12}$$

where $\alpha = \alpha(s)$ is the angle between the axis Ox_1 and the tangent at the point $\xi \in L$, and taking into account that for the circle

$$\exp(i\alpha) = \exp[i(\beta + \pi/2)] = i\frac{\tau}{R},$$
(13)

where $\beta = \beta(s)$ is the angle between the axis Ox_1 and the normal to the arc at the point characterized by complex variable $\tau(s)$, one can rewrite Eqs. (4)-(6), in complex variables notations as

$$\sigma^S = \sigma_0 + (\lambda_S + 2\mu_S)\varepsilon^S = \sigma_0 + (\lambda_S + 2\mu_S)\operatorname{Re} u', \tag{14a}$$

$$\varepsilon^S = \frac{u_n}{R} + \frac{\partial u_\ell}{\partial s} = \text{Re}\,u',$$
 (14b)

$$\omega^S = -\frac{u_\ell}{R} + \frac{\partial u_n}{\partial s} = -\operatorname{Im} u', \tag{14c}$$

3 REPRESENTATION OF THE GEOMETRY AND FIELDS BY COMPLEX VARIABLES7 where u' is defined as follows:

$$u' = \frac{\mathrm{d}u}{\mathrm{d}\tau} + \frac{\mathrm{d}\bar{\tau}}{\mathrm{d}\tau} \frac{\mathrm{d}u}{\mathrm{d}\bar{\tau}}.\tag{15}$$

3.2. Complex variables integral representations for the fields

The integral representations for the elastic fields in the material system under study can be deduced from the representations for more general case of a curve of an arbitrary shape, see Linkov and Mogilevskaya (1998), Mogilevskaya and Linkov (1998), Mogilevskaya et al. (2021a,b), Zemlyanova et al. (2023).

The representation for the complex displacements outside of L is

$$u(z) = u^{\infty}(z) - \frac{1}{4\pi i \mu (\kappa + 1)} \left\{ \int_{L} \Delta \sigma(\tau) \left[2\kappa \ln(z - \tau) - \kappa K_{1}(\tau, z) \right] d\tau + \int_{L} \overline{\Delta \sigma(\tau)} K_{2}(\tau, z) d\overline{\tau} \right\},$$

$$(16)$$

in which $z=x_1+\mathrm{i} x_2$ is the complex combination of the Cartesian coordinates of the point $z\notin L,\,\Delta\sigma=\Delta\sigma_n+\mathrm{i}\Delta\sigma_\ell,\,\kappa=3-4\nu,$

$$K_1(\tau, z) = \ln \frac{\tau - z}{\overline{\tau} - \overline{z}}, \quad K_2(\tau, z) = \frac{\tau - z}{\overline{\tau} - \overline{z}}, \tag{17}$$

and

$$u^{\infty}(z) = \frac{1}{2\mu} \left[(\kappa - 1) \frac{\sigma_{11}^{\infty} + \sigma_{22}^{\infty}}{4} z - \frac{\sigma_{22}^{\infty} - \sigma_{11}^{\infty} - 2i\sigma_{12}^{\infty}}{2} \overline{z} \right].$$
 (18)

The expressions for the complex tractions on some line outside of L is

$$\sigma(z) = \sigma^{\infty}(z) - \frac{1}{2\pi i (\kappa + 1)} \left\{ \int_{L} \Delta \sigma(\tau) \left[(\kappa - 1) \frac{1}{\tau - z} + \kappa \frac{\partial}{\partial z} K_{1}(\tau, z) \right] d\tau - \int_{L} \overline{\Delta \sigma(\tau)} \frac{\partial}{\partial z} K_{2}(\tau, z) d\overline{\tau} \right\},$$
(19)

3 REPRESENTATION OF THE GEOMETRY AND FIELDS BY COMPLEX VARIABLES8 where

$$\sigma^{\infty}(z) = \frac{\sigma_{11}^{\infty} + \sigma_{22}^{\infty}}{2} + \frac{\sigma_{22}^{\infty} - \sigma_{11}^{\infty} - 2i\sigma_{12}^{\infty}}{2} \frac{\mathrm{d}\overline{z}}{\mathrm{d}z}.$$
 (20)

As in Mogilevskaya et al. (2021b), Zemlyanova et al. (2023), the boundary integral equation will be obtained using the following representation that results from Eqs. (15), (16):

$$u'(z) = \left[u^{\infty}(z)\right]' + \frac{1}{4\pi i \mu (\kappa + 1)} \left\{ \int_{L} \Delta \sigma (\tau) \left[2\kappa \frac{1}{\tau - z} + \kappa \frac{\partial}{\partial z} K_{1}(\tau, z) \right] d\tau - \int_{L} \overline{\Delta \sigma (\tau)} \frac{\partial}{\partial z} K_{2}(\tau, z) d\overline{\tau} \right\},$$
(21)

where

$$[u^{\infty}(z)]' = \frac{1}{2\mu} \left[(\kappa - 1) \frac{\sigma_{11}^{\infty} + \sigma_{22}^{\infty}}{4} - \frac{\sigma_{22}^{\infty} - \sigma_{11}^{\infty} - 2i\sigma_{12}^{\infty}}{2} \frac{d\overline{z}}{dz} \right].$$
 (22)

3.3. Boundary integral equation in terms of complex variables

Using the limiting procedure in which the field point is allowed to reach the boundary point $\tau^0 = \tau_1^0 + i\tau_2^0$ from the direction normal to the boundary at that point, the following boundary integral equation is obtained, see Mogilevskaya et al. (2021b), Zemlyanova et al. (2023):

$$u'(\tau^{0}) = \left[u^{\infty}(\tau^{0})\right]' + \frac{1}{4\pi i \mu(\kappa+1)} \left\{ \int_{L} \Delta \sigma(\tau) \left[2\kappa \frac{1}{\tau - \tau^{0}} + \kappa \frac{\partial}{\partial \tau^{0}} K_{1}(\tau, \tau^{0}) \right] d\tau - \int_{L} \overline{\Delta \sigma(\tau)} \frac{\partial}{\partial \tau^{0}} K_{2}(\tau, \tau^{0}) d\bar{\tau} \right\}.$$
(23)

Using Eqs. (8), (17), we get for the points on L

$$K_1 = \ln \frac{(\tau - \tau^0)\tau\tau^0}{R^2(\tau^0 - \tau)} = \ln \left(-\frac{\tau\tau^0}{R^2}\right), \ K_2 = -\frac{\tau\tau^0}{R^2},$$
 (24a)

$$d\bar{\tau} = -\frac{R^2}{\tau^2}d\tau, \quad \frac{\partial K_1}{\partial \tau^0} = \frac{1}{\tau^0}, \quad \frac{\partial K_2}{\partial \tau^0} = -\frac{\tau}{R^2}.$$
 (24b)

Substituting the expressions of Eq. (24) into Eq. (23), we obtain the following boundary integral equation:

$$u'(\tau^0) = u^{\infty}(\tau^0)' + \frac{1}{4\pi i\mu(\kappa+1)} \left[\int_L \Delta\sigma(\tau) \left(2\kappa \frac{1}{\tau - \tau^0} + \kappa \frac{1}{\tau^0} \right) d\tau - \int_L \overline{\Delta\sigma(\tau)} \frac{1}{\tau} d\tau \right]. \quad (25)$$

4. The system of hypersingular boundary integral equations

4.1. Reduction of Eq. (25) to the system of real variables equations

Using the following representations for the points on L:

$$\tau = Re^{i\beta}, \ \tau^0 = Re^{i\beta_0}, \ d\tau = iRe^{i\beta}d\beta, \ \frac{d\bar{\tau}_0}{d\tau_0} = \frac{d}{d\tau_0}\frac{R^2}{\tau_0} = -e^{-2i\beta_0},$$
 (26)

and substituting Eq. (26) into Eq. (25), we get (here and below, we omitted the arguments τ^0 and τ for brevity)

$$u' = u^{\infty'} + \frac{\kappa}{2\pi\mu(\kappa+1)} \int_{L} (\Delta\sigma_n + i\Delta\sigma_\ell) \frac{e^{i\beta}}{e^{i\beta} - e^{i\beta_0}} d\beta$$
$$+ \frac{\kappa}{4\pi\mu(\kappa+1)} \int_{L} (\Delta\sigma_n + i\Delta\sigma_\ell) e^{i(\beta-\beta_0)} d\beta$$
$$- \frac{1}{4\pi\mu(\kappa+1)} \int_{L} (\Delta\sigma_n - i\Delta\sigma_\ell) d\beta.$$
(27)

Taking into account that

$$\frac{e^{i\beta}}{e^{i\beta} - e^{i\beta_0}} = \frac{1}{2} - i \frac{\sin(\beta - \beta_0)}{2[1 - \cos(\beta - \beta_0)]}, \ e^{i(\beta - \beta_0)} = \cos(\beta - \beta_0) + i \sin(\beta - \beta_0), \tag{28}$$

and using Eqs. (2), (3), (12), (13), (14a), (14c), (27), (28), one can arrive, after some algebra,

at the following system of real variables integral equations in terms of σ^S and ω^S :

$$\sigma^{S} = (\lambda_{S} + 2\mu_{S}) \operatorname{Re} u^{\infty \prime} + \sigma_{0}$$

$$+ \frac{\lambda_{S} + 2\mu_{S}}{4\pi R \mu(\kappa + 1)} \int_{\beta_{1}}^{\beta_{2}} \left[\kappa \frac{\sigma^{S} \cos(\beta - \beta_{0}) + \sigma_{0} \omega^{S} \sin(\beta - \beta_{0})}{1 - \cos(\beta - \beta_{0})} + \sigma^{S} \right] d\beta,$$
(29)

$$\omega^{S} = -\operatorname{Im} u^{\infty'} + \frac{1}{4\pi R\mu(\kappa+1)} \int_{\beta_{1}}^{\beta_{2}} \left[\kappa \frac{\sigma_{0} \omega^{S} \cos(\beta - \beta_{0}) - \sigma^{S} \sin(\beta - \beta_{0})}{1 - \cos(\beta - \beta_{0})} - \sigma_{0} \omega^{S} \right] d\beta, (30)$$

where β_1 and β_2 are the angles associated with the tips of L and $\operatorname{Re} u^{\infty'}$, $\operatorname{Im} u^{\infty'}$ are obtained from Eqs. (22), (26) as

$$\operatorname{Re} u^{\infty'} = \frac{1}{2\mu} \left[(\kappa - 1) \frac{\sigma_{11}^{\infty} + \sigma_{22}^{\infty}}{4} - \frac{2\sigma_{12}^{\infty} \sin(2\beta_0) + \cos(2\beta_0)(\sigma_{11}^{\infty} - \sigma_{22}^{\infty})}{2} \right],$$

$$\operatorname{Im} u^{\infty'} = \frac{1}{2\mu} \left[\frac{\sigma_{11}^{\infty} - \sigma_{22}^{\infty}}{2} \sin(2\beta_0) - \sigma_{12}^{\infty} \cos(2\beta_0) \right].$$
(31)

4.2. Dimensionless integral equations

Introducing the following dimensionless parameters

$$\theta = \beta_2 - \beta_1, \ \tilde{\sigma}_{ij}^{\infty} = \frac{\sigma_{ij}^{\infty}}{\mu}, \ \gamma = \frac{\mu R \theta}{2\mu_S + \lambda_S}, \ \tilde{\sigma}^S = \frac{2\sigma^S}{\mu R \theta}, \ \tilde{\sigma}_0 = \frac{2\sigma_0}{\mu R \theta},$$
 (32)

one can re-write Eq. (29) and Eq. (30) as follows:

$$\gamma \tilde{\sigma}^{S} = \Sigma_{1} + \gamma \tilde{\sigma}_{0} + \frac{\theta/2}{2\pi(\kappa + 1)} \int_{\beta_{1}}^{\beta_{2}} \tilde{\sigma}^{S} d\beta$$

$$+ \frac{\kappa \theta/2}{2\pi(\kappa + 1)} \int_{\beta_{1}}^{\beta_{2}} \frac{\tilde{\sigma}^{S} \cos(\beta - \beta_{0}) + \tilde{\sigma}_{0} \omega^{S} \sin(\beta - \beta_{0})}{1 - \cos(\beta - \beta_{0})} d\beta,$$
(33)

$$\omega^{S} = -\Sigma_{2} - \frac{\tilde{\sigma}_{0}\theta/2}{4\pi(\kappa+1)} \int_{\beta_{1}}^{\beta_{2}} \omega^{S} d\beta + \frac{\kappa\theta/2}{4\pi(\kappa+1)} \int_{\beta_{1}}^{\beta_{2}} \frac{\tilde{\sigma}_{0}\omega^{S} \cos(\beta-\beta_{0}) - \tilde{\sigma}^{S} \sin(\beta-\beta_{0})}{1 - \cos(\beta-\beta_{0})} d\beta.$$
(34)

where

$$\Sigma_{1} = (\kappa - 1) \frac{\tilde{\sigma}_{11}^{\infty} + \tilde{\sigma}_{22}^{\infty}}{4} - \frac{2\tilde{\sigma}_{12}^{\infty} \sin(2\beta_{0}) + \cos(2\beta_{0})(\tilde{\sigma}_{11}^{\infty} - \tilde{\sigma}_{22}^{\infty})}{2},$$

$$\Sigma_{2} = \frac{\tilde{\sigma}_{11}^{\infty} - \tilde{\sigma}_{22}^{\infty}}{4} \sin(2\beta_{0}) - \frac{\tilde{\sigma}_{12}^{\infty}}{2} \cos(2\beta_{0}).$$
(35)

Using the linear transformation

$$\beta = \frac{\theta}{2}\bar{\beta} + b,\tag{36}$$

in which $b = (\beta_1 + \beta_2)/2$, the integrals involved in Eqs. (33) and (34) can be transformed to those over the interval $\bar{\beta} \in [-1, 1]$ and the resulting equations become

$$-\Sigma_{1} - \gamma \tilde{\sigma}_{0} = -\gamma \tilde{\sigma}^{S}(\bar{\beta}_{0}) + \frac{(1-\kappa)\theta^{2}}{8\pi(\kappa+1)} \int_{-1}^{1} \tilde{\sigma}^{S}(\bar{\beta}) d\bar{\beta} + \frac{\kappa \theta^{2}}{8\pi(\kappa+1)} \int_{-1}^{1} \frac{\tilde{\sigma}^{S}(\bar{\beta}) + \tilde{\sigma}_{0} \omega^{S}(\bar{\beta}) \sin[\theta/2(\bar{\beta} - \bar{\beta}_{0})]}{1 - \cos[\theta/2(\bar{\beta} - \bar{\beta}_{0})]} d\bar{\beta},$$
(37)

$$\Sigma_{2} = -\omega^{S}(\bar{\beta}_{0}) - \frac{\tilde{\sigma}_{0}\theta^{2}}{16\pi} \int_{-1}^{1} \omega^{S}(\bar{\beta}) d\bar{\beta} + \frac{\kappa\theta^{2}}{16\pi(\kappa+1)} \int_{-1}^{1} \frac{\tilde{\sigma}_{0}\omega^{S}(\bar{\beta}) - \tilde{\sigma}^{S}(\bar{\beta}) \sin[\theta/2(\bar{\beta} - \bar{\beta}_{0})]}{1 - \cos[\theta/2(\bar{\beta} - \bar{\beta}_{0})]} d\bar{\beta}.$$
(38)

5. Numerical solution

5.1. Approximations of the unknown functions

On a circular arc, it is reasonable to approximate sufficiently smooth functions by truncated series of trigonometric functions. To account for the tip conditions of Eq. (7), we suggest to use the square root weight function, as in Mogilevskaya et al. (2021b), Zemlyanova et al. (2023).

Thus, the approximations for $\tilde{\sigma}^S(\beta)$ and $\omega^S(\beta)$ are taken as

$$\tilde{\sigma}^{S}(\beta) = \sqrt{(\beta - \beta_1)(\beta - \beta_2)} \sum_{m=0}^{N} \left[A_m \cos(m\beta) + B_m \sin(m\beta) \right],$$

$$\omega^{S}(\beta) = \sqrt{(\beta - \beta_1)(\beta - \beta_2)} \sum_{m=0}^{N} \left[D_m \cos(m\beta) + E_m \sin(m\beta) \right].$$
(39)

Approximations of Eq. (39) can be further reduced to the following ones written in terms of $\bar{\beta}$ (after we omit the constant multiplier in the weight function):

$$\tilde{\sigma}^{S}(\bar{\beta}) = \sqrt{1 - \bar{\beta}^{2}} \sum_{m=0}^{N} \left\{ A_{m} \cos[m(\theta/2\bar{\beta} + b)] + B_{m} \sin[m(\theta/2\bar{\beta} + b)] \right\}$$

$$= \sqrt{1 - \bar{\beta}^{2}} \sum_{m=0}^{N} \left\{ A_{m} \cos[m\theta/2(\bar{\beta} - \bar{\beta}_{0}) + m(\theta/2\bar{\beta}_{0} + b)] + B_{m} \sin[m\theta/2(\bar{\beta} - \bar{\beta}_{0}) + m(\theta/2\bar{\beta}_{0} + b)] \right\}$$

$$= \sqrt{1 - \bar{\beta}^{2}} \sum_{m=0}^{N} \left\{ A_{m} [\cos(2mt)\cos(mg) - \sin(2mt)\sin(mg)] + B_{m} [\sin(2mt)\cos(mg) + \cos(2mt)\sin(mg)] \right\},$$
(40a)

$$\omega^{S}(\bar{\beta}) = \sqrt{1 - \bar{\beta}^{2}} \sum_{m=0}^{N} \left\{ D_{m} \cos[m(\theta/2\bar{\beta} + b)] + E_{m} \sin[m(\theta/2\bar{\beta} + b)] \right\}$$

$$= \sqrt{1 - \bar{\beta}^{2}} \sum_{m=0}^{N} \left\{ D_{m} \cos[m\theta/2(\bar{\beta} - \bar{\beta}_{0}) + m(\theta/2\bar{\beta}_{0} + b)] + E_{m} \sin[m\theta/2(\bar{\beta} - \bar{\beta}_{0}) + m(\theta/2\bar{\beta}_{0} + b)] \right\}$$

$$= \sqrt{1 - \bar{\beta}^{2}} \sum_{m=0}^{N} \left\{ D_{m} [\cos(2mt) \cos(mg) - \sin(2mt) \sin(mg)] + E_{m} [\sin(2mt) \cos(mg) + \cos(2mt) \sin(mg)] \right\},$$
(40b)

where A_m , B_m , D_m , and E_m are unknown coefficients for the m-th terms in truncated series and

$$t = t(\bar{\beta}) = \theta/4(\bar{\beta} - \bar{\beta}_0), \ g = g(\bar{\beta}_0) = \theta\bar{\beta}_0/2 + b.$$
 (41)

13

5.2. Evaluation of the integrals

5.2.1. List of integrals

Substitution of the approximations of Eq. (40) into the system of Eqs. (37), (38) (with the use of the variables introduced in Eq. (41)) produces integrals of the following types:

$$I_{1}^{m} = \int_{-1}^{1} \sqrt{1 - \bar{\beta}^{2}} \cos(2mt) d\bar{\beta},$$

$$I_{2}^{m} = \int_{-1}^{1} \sqrt{1 - \bar{\beta}^{2}} \sin(2mt) d\bar{\beta},$$

$$I_{3}^{m} = \int_{-1}^{1} \sqrt{1 - \bar{\beta}^{2}} \frac{\sin(2mt) \sin 2t}{1 - \cos(2t)} d\bar{\beta} = \int_{-1}^{1} \sqrt{1 - \bar{\beta}^{2}} \frac{\sin(2mt)}{\tan t} d\bar{\beta},$$

$$I_{4}^{m} = \int_{-1}^{1} \sqrt{1 - \bar{\beta}^{2}} \frac{\cos(2mt)}{1 - \cos(2t)} d\bar{\beta},$$

$$I_{5}^{m} = \int_{-1}^{1} \sqrt{1 - \bar{\beta}^{2}} \frac{\sin(2mt)}{1 - \cos(2t)} d\bar{\beta},$$

$$I_{6}^{m} = \int_{-1}^{1} \sqrt{1 - \bar{\beta}^{2}} \frac{\cos(2mt) \sin 2t}{1 - \cos(2t)} d\bar{\beta} = \int_{-1}^{1} \sqrt{1 - \bar{\beta}^{2}} \frac{\cos(2mt)}{\tan t} d\bar{\beta},$$

$$(42)$$

where superscript m in I_i^m $(i=1,\cdots,6)$ denotes the integral related to the m-th term in truncated series.

It can be easily seen that the integrals I_1^m and I_2^m in Eq. (42) are regular integrals, which can be directly evaluated by the Gaussian quadrature. To determine the singularities of the remaining integrals, one has to investigate the behavior of their integrands when $t \to 0$, i.e., $\bar{\beta} \to \bar{\beta}_0$. Such investigation reveals that I_3^m is also a regular integral, since the denominator $\tan t$ behaves as t when $t \to 0$, while numerator $\sin(2mt)$ at the same time behaves as (2mt), leading to the limiting value of the integrand to be $2m\sqrt{1-\bar{\beta}^2}$, which is a regular function.

5.2.2. Singular behavior of the remaining integrals of Eq. (42)

We will now demonstrate that the integral I_4^m of Eq. (42) can be represented as,

$$I_4^m = \int_{-1}^1 \sqrt{1 - \bar{\beta}^2} \left[\frac{\cos(2mt)}{1 - \cos(2t)} - \frac{1}{2t^2} \right] d\bar{\beta} + \frac{1}{2} \int_{-1}^1 \frac{\sqrt{1 - \bar{\beta}^2}}{t^2} d\bar{\beta}, \tag{43}$$

in which the first term on the right-hand side is the regular integral while the second term is the so-called hypersingular integral, see e.g. Lin'kov and Mogilevskaya (1990), Martin (1992).

To prove that the first integral is regular, we represent the numerator and denominators of the first term in the brackets of Eq. (43) by the truncated Taylor series and obtain the following result:

$$\int_{-1}^{1} \sqrt{1 - \bar{\beta}^{2}} \left[\frac{\cos(2mt)}{1 - \cos(2t)} - \frac{1}{2t^{2}} \right] d\bar{\beta}$$

$$= \int_{-1}^{1} \sqrt{1 - \bar{\beta}^{2}} \left[\frac{1 - \frac{(2mt)^{2}}{2!} + \mathcal{O}(t^{4})}{\frac{(2t)^{2}}{2!} + \mathcal{O}(t^{4})} - \frac{1}{2t^{2}} \right] d\bar{\beta}$$

$$= \int_{-1}^{1} \sqrt{1 - \bar{\beta}^{2}} \frac{1 - \frac{(2mt)^{2}}{2!} + \mathcal{O}(t^{4}) - 1 + \frac{1}{3}t^{2} + \mathcal{O}(t^{4})}{2t^{2} \left[1 + \mathcal{O}(t^{2})\right]} d\bar{\beta}$$

$$= \int_{-1}^{1} \sqrt{1 - \bar{\beta}^{2}} \left(-m^{2} + \frac{1}{6} \right) \frac{1 + \mathcal{O}(t^{2})}{1 + \mathcal{O}(t^{2})} d\bar{\beta}$$
(44)

It is easy to see that that the kernel of the final expression of Eq. (44) has finite limit value of $(-m^2 + 1/6)\sqrt{1 - \bar{\beta}^2}$ when $t \to 0$ and, thus, the first integral of Eq. (43) is regular.

The second, hypersingular, integral of Eq. (43) can be evaluated analytically as, see Martin (1992)

$$\oint_{-1}^{1} \frac{\sqrt{1-\bar{\beta}^2}}{t^2} d\bar{\beta} = \oint_{-1}^{1} \frac{\sqrt{1-\bar{\beta}^2}}{\left[\theta/4(\bar{\beta}-\bar{\beta}_0)\right]^2} d\bar{\beta} = \frac{16}{\theta^2} \oint_{-1}^{1} \frac{\sqrt{1-\bar{\beta}^2}}{\left(\bar{\beta}-\bar{\beta}_0\right)^2} d\bar{\beta} = -\frac{16}{\theta^2} \pi.$$
(45)

Similarly, we represent the integral I_5^m as,

$$I_5^m = \int_{-1}^1 \sqrt{1 - \bar{\beta}^2} \left[\frac{\sin(2mt)}{1 - \cos(2t)} - \frac{m}{t} \right] d\bar{\beta} + m \int_{-1}^1 \frac{\sqrt{1 - \bar{\beta}^2}}{t} d\bar{\beta}, \tag{46}$$

where the first term on the right hand side of Eq. (46) is the regular integral, as it can be proved (as it was done for I_4^m) that the limit value of its kernel is 0 when $t \to 0$. The second term on the right hand side of Eq. (46) is the singular Cauchy type integral and it can be

evaluated analytically as, see Martin (1992),

$$\int_{-1}^{1} \frac{\sqrt{1 - \bar{\beta}^2}}{t} d\bar{\beta} = \int_{-1}^{1} \frac{\sqrt{1 - \bar{\beta}^2}}{\theta / 4(\bar{\beta} - \bar{\beta}_0)} d\bar{\beta} = \frac{4}{\theta} \int \frac{\sqrt{1 - \bar{\beta}^2}}{\bar{\beta} - \bar{\beta}_0} d\bar{\beta} = -\frac{4}{\theta} \bar{\beta}_0 \pi. \tag{47}$$

Finally, the integral I_6^m can be treated as,

$$I_6^m = \int_{-1}^1 \sqrt{1 - \bar{\beta}^2} \left[\frac{\cos(2mt)}{\tan t} - \frac{1}{t} \right] d\bar{\beta} + \int_{-1}^1 \frac{\sqrt{1 - \bar{\beta}^2}}{t} d\bar{\beta}$$
 (48)

where the first term on the right hand side of Eq. (48) is the regular integral, as it can be proved that its kernel has the limit value of 0 when $t \to 0$, while the second term is Cauchy type singular integral, which can be evaluated using Eq. (47).

5.2.3. Treatments of regular integrals

Regular integrals I_1^m , I_2^m , I_3^m of Eq. (42) and the first integrals on the right hand sides of Eqs. (43), (46) and (48) are evaluated numerically using Gaussian quadrature.

GP	m=0	m=10	m=20	m=30	m=40
20	0.26438	-67.5035	-144.851	-222.256	-299.658
50	0.26437	-67.5033	-144.851	-222.256	-299.668
100	0.26437	-67.5033	-144.851	-222.256	-299.668
200	0.26437	-67.5033	-144.851	-222.256	-299.668
400	0.26437	-67.5033	-144.851	-222.256	-299.668
800	0.26437	-67.5032	-144.851	-222.255	-299.668

Table 1: Convergence analysis of regular integral in Eq. (43) for $\bar{\beta}_0 = 0.25$.

The results of the convergence analysis for the regular integral of Eq. (43) are presented in Table 1 in which "GP" denotes the number of Gaussian points and m is the truncation number. The arc of unit radius is characterized by the angles $\beta_1 = \pi/4$, $\beta_2 = 3\pi/4$ and the value of $\bar{\beta}_0$ is taken to be $\bar{\beta}_0 = 0.25$. In cases of large m, some of the Gaussian points are located very close to the origin. In order to evaluate the values of the kernel at such points accurately, we expanded the latter into Taylor series up to at least $\mathcal{O}(t^{11})$ when $|\bar{\beta}_0 - \bar{\beta}| \leq 0.1$.

From the results of Table 1, it can be concluded that 100 Gaussian points are sufficient for accurate numerical evaluation of the regular integral of Eq. (43).

Similar results are presented in Table 2 for the regular integral of Eq. (46) and the same values of β_1 , β_2 , and $\bar{\beta}_0$. Here too, 100 Gaussian points are sufficient for accurate numerical evaluation of the regular integral of Eq. (46).

GP	m=0	m = 10	m = 20	m = 30	m = 40
20	0.00000	17.2649	37.4370	57.3773	77.3928
50	0.00000	17.2656	37.4384	57.3793	77.4143
100	0.00000	17.2656	37.4385	57.3794	77.4145
200	0.00000	17.2656	37.4385	57.3794	77.4145
400	0.00000	17.2656	37.4385	57.3794	77.4145
800	0.00000	17.2656	37.4385	57.3794	77.4145

Table 2: Convergence analysis of regular integral in Eq. (46) related to $\bar{\beta}_0 = 0.25$.

To ensure that all regular integrals are accurately evaluated, we implemented 800 Gaussian points in all numerical examples considered below.

5.2.4. Reduction to linear system equations

Standard collocation method is used to generate the system of linear algebraic equations from the governing integral equations of Eq. (37) and Eq. (38).

If the series in Eq. (40) are truncated at m = N, the total number of unknown coefficients in approximations for $\tilde{\sigma}^S$ and ω^S is 4(N+1). To obtain these coefficients, 2(N+1) collocation points are required. They are chosen to be uniformly distributed on the circular arc L away from its tips, since the approximations of Eq. (40) already satisfy the tip conditions of Eq. (7).

Substituting the approximations of Eq. (40) into the governing equations of Eq. (37), Eq. (38) and evaluating all integrals of Eq. (42), we obtain the following system of linear

algebraic equations for each collocation point $\bar{\beta}_{0j}$, where $j=1,\cdots,2(N+1)$,

$$-\gamma \tilde{\sigma}_{0} - \Sigma_{1j} = -\gamma \tilde{\sigma}^{S}(\bar{\beta}_{0j}) + \frac{(1-\kappa)\theta^{2}}{8\pi(\kappa+1)} \sum_{m=0}^{N} \left\{ A_{m} \left[\cos(mg_{j})I_{1j}^{m} - \sin(mg_{j})I_{2j}^{m} \right] + B_{m} \left[\cos(mg_{j})I_{2j}^{m} + \sin(mg_{j})I_{1j}^{m} \right] \right\} + \frac{\kappa\theta^{2}}{8\pi(\kappa+1)} \sum_{m=0}^{N} \left\{ A_{m} \left[\cos(mg_{j})I_{4j}^{m} - \sin(mg_{j})I_{5j}^{m} \right] + B_{m} \left[\cos(mg_{j})I_{5j}^{m} + \sin(mg_{j})I_{4j}^{m} \right] \right\} + \frac{\kappa\theta^{2}\tilde{\sigma}_{0}}{8\pi(\kappa+1)} \sum_{m=0}^{N} \left\{ D_{m} \left[\cos(mg_{j})I_{6j}^{m} - \sin(mg_{j})I_{3j}^{m} \right] + E_{m} \left[\cos(mg_{j})I_{3j}^{m} + \sin(mg_{j})I_{6j}^{m} \right] \right\},$$

$$(49a)$$

$$\Sigma_{2j} = -\omega^{S}(\bar{\beta}_{0j}) + \frac{\kappa\theta^{2}\tilde{\sigma}_{0}}{16\pi(\kappa+1)} \sum_{m=0}^{N} \left\{ D_{m} \left[\cos(mg_{j})I_{4j}^{m} - \sin(mg_{j})I_{5j}^{m} \right] + E_{m} \left[\cos(mg_{j})I_{5j}^{m} + \sin(mg_{j})I_{4j}^{m} \right] \right\} - \frac{\kappa\theta^{2}}{16\pi(\kappa+1)} \sum_{m=0}^{N} \left\{ A_{m} \left[\cos(mg_{j})I_{6j}^{m} - \sin(mg_{j})I_{3j}^{m} \right] + B_{m} \left[\cos(mg_{j})I_{3j}^{m} + \sin(mg_{j})I_{6j}^{m} \right] \right\} - \frac{\tilde{\sigma}_{0}\theta^{2}}{16\pi} \sum_{m=0}^{N} \left\{ D_{m} \left[\cos(mg_{j})I_{1j}^{m} - \sin(mg_{j})I_{2j}^{m} \right] + E_{m} \left[\cos(mg_{j})I_{2j}^{m} + \sin(mg_{j})I_{1j}^{m} \right] \right\}.$$

$$(49b)$$

in which $g_j = \theta \bar{\beta}_{0j}/2 + b$, Σ_{1j} , Σ_{2j} of Eq. (35) and integrals I_{1j}^m of Eq. (42) are all evaluated at the *j*-th collocation point $\bar{\beta}_{0j}$.

After solving the system of equations Eq. (49a), Eq. (49b), one can obtain the coefficients A_m , B_m , D_m , and E_m . Substitution of those coefficients into the approximations of Eq. (40) provides the values of $\tilde{\sigma}^S$ and ω^S on the arc L. The jumps $\Delta \tilde{\sigma} = \Delta \sigma/\mu$ can be then evaluated using Eqs. (2), (3).

The tractions $\sigma(z) = \sigma_n(z) + i\sigma_\ell(z)$ outside of L are evaluated using Eq. (19), while the Cauchy stresses σ_{ij} are evaluated using Eq. (19) with the set of appropriately chosen normal vectors. For example, to calculate $\sigma_{11}(z)$ and $\sigma_{12}(z)$, one can set $z = ix_2$ and assume that normal vector to the line on which z is located (axis Ox_2) points in Ox_1 direction. Thus, $\sigma_n(z) = \sigma_{11}(z)$ and $\sigma_\ell(z) = \sigma_{12}(z)$ on that line. Similarly, to obtain σ_{22} , one can set

6 COMPARISON WITH THE SOLUTION FOR THE RIGID CIRCULAR ARC PROBLEM18 $z=x_1$ and assume that the normal to the line on which z is located (axis Ox_1) points in Ox_2 direction leading to $\sigma_{22}=\sigma_n$ on that line.

6. Comparison with the solution for the rigid circular arc problem

It was shown in Mogilevskaya et al. (2021b) that the problem of the Gurtin-Murdoch material surface (in plane strain setting) is reduced to that of a rigid line (stiffener) in the case of L being a straight segment and $\gamma = 0$, $\sigma_0 = 0$.

We now will demonstrate that this is not the case for the circular arc problem considered here. To do so, we analyze the solution of Liu and Jiang (1994) for the problem of a rigid circular arc embedded into an infinite isotropic elastic plane.

For simplicity, we consider a special case of uniaxial load σ_{11}^{∞} for which $\varepsilon = 0$, see Eq. (62) in Liu and Jiang (1994). Using the expressions for the complex potentials of Eqs. (15), (55)-(56) in Liu and Jiang (1994), we first obtain the limit values of complex tractions at the arc boundary ($\tau \bar{\tau} = R^2$). Subtraction of these limit values leads to the following expression for the complex traction jump across the rigid arc:

$$\Delta \sigma = \chi_0^+(\tau) \frac{\kappa + 1}{\kappa} \left[-\frac{R^3 \bar{\Gamma}'}{\tau^2} + \frac{R^3 \bar{\Gamma}'}{\tau^2} \cos \frac{\theta}{2} + (\kappa \Gamma - D) \left(\tau - R \cos \frac{\theta}{2} \right) \right], \tag{50}$$

in which

$$\chi_0^+(\tau) = -\chi_0^-(\tau) = -\frac{1}{\sqrt{(Re^{i\beta} + Ri)(Re^{i\beta} - Ri)}} = -\frac{1}{R\sqrt{e^{2i\beta} + 1}} = -\frac{e^{-i\beta/2}}{R\sqrt{2\cos\beta}}, \quad (51)$$

and the meaning of the remaining parameters is explained in Liu and Jiang (1994).

Assuming that $\theta = \beta_2 - \beta_1 = \pi$ and taking into account that, for uniaxial load, see Eqs. (59)-(61) in Liu and Jiang (1994),

$$\Gamma = \frac{\sigma_{11}^{\infty}}{4}, \ \bar{\Gamma}' = -\frac{\sigma_{11}^{\infty}}{2}, \ D = \frac{\sigma_{11}^{\infty}}{4} \frac{\kappa + 1}{2\kappa - 1}, \ \cos\frac{\theta}{2} = 0,$$
 (52)

6 COMPARISON WITH THE SOLUTION FOR THE RIGID CIRCULAR ARC PROBLEM19 we get, after substituting Eqs. (51), (52) into Eq. (50), that

$$\Delta\sigma = -\frac{\kappa + 1}{2\kappa} \frac{\sigma_{11}^{\infty}}{\sqrt{2\cos\beta}} \left[e^{-i5\beta/2} + \frac{2\kappa^2 - 2\kappa - 1}{2(2\kappa - 1)} e^{i\beta/2} \right]. \tag{53}$$

Therefore, the jumps in traction components across the rigid arc in the solution of Liu and Jiang (1994) are,

$$\Delta \sigma_n = -\frac{\kappa + 1}{2\kappa} \frac{\sigma_{11}^{\infty}}{\sqrt{2\cos\beta}} \left[\cos\left(\frac{5}{2}\beta\right) + \frac{2\kappa^2 - 2\kappa - 1}{2(2\kappa - 1)} \cos\left(\frac{\beta}{2}\right) \right],\tag{54a}$$

$$\Delta \sigma_{\ell} = \frac{\kappa + 1}{2\kappa} \frac{\sigma_{11}^{\infty}}{\sqrt{2\cos\beta}} \left[\sin\left(\frac{5}{2}\beta\right) - \frac{2\kappa^2 - 2\kappa - 1}{2(2\kappa - 1)} \sin\left(\frac{\beta}{2}\right) \right]. \tag{54b}$$

If we take $\sigma_0 = 0$ and $\gamma = 0$ in the Gurtin-Murdoch theory, we get (according to Eqs. (2) and (3) of the present paper) that

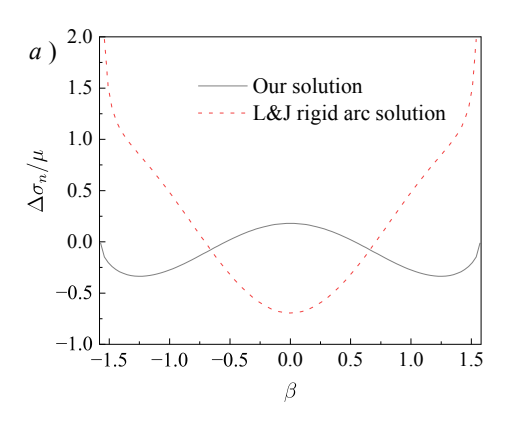
$$\Delta \sigma_n = -\frac{\sigma^S}{R}, \ \Delta \sigma_\ell = \frac{\partial \sigma^S}{\partial s} = \frac{1}{R} \frac{\partial \sigma^S}{\partial \beta} = -\frac{\partial}{\partial \beta} \Delta \sigma_n. \tag{55}$$

It can be seen that jumps in traction components of Eq. (54) resulted from the rigid arc solution of Liu and Jiang (1994) do not satisfy the second condition of Eq. (55).

This fact can be explained using the Benveniste and Miloh classification of thin interphase layers, i.e. Benveniste and Miloh (2001), in which the Gurtin-Murdoch jump conditions and those for the rigid interface describe two distinct interface regimes, see Eqs. (2.11), (2.17) in Benveniste and Miloh (2001).

It is interesting to compare the dimensionless jumps $\Delta \sigma_n/\mu$ and $\Delta \sigma_\ell/\mu$ obtained using the solution of Liu and Jiang (1994) with the ones obtained from the Gurtin-Murdoch theory with $\sigma_0 = 0$ and $\gamma = 0$. The following parameters are chosen for the comparison: $\sigma_{11}^{\infty}/\mu = 1$, $\nu = 0.35$, R = 1, and $\beta \in [-\pi/2, \pi/2]$. The corresponding results are plotted on Fig. 2.

It should be seen from Fig. 2a that $\Delta \sigma_n/\mu = 0$ for our solution when $\beta = -\pi/2$ or



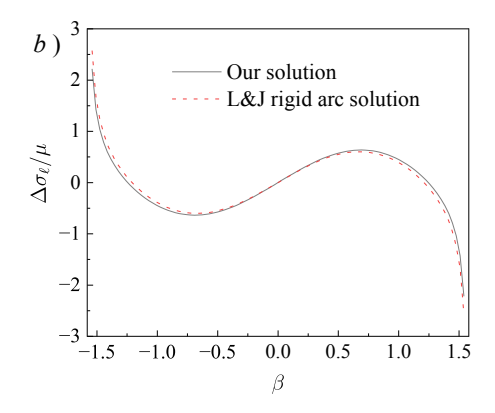


Figure 2: Comparisons of stresses jumps $\Delta \sigma_n/\mu$ and $\Delta \sigma_\ell/\mu$ obtained using the Gurtin-Murdoch theory with $\sigma_0 = 0$, $\gamma = 0$ and the ones by Liu and Jiang (1994).

 $\beta = \pi/2$, while the the corresponding values calculated using the solution by Liu and Jiang (1994) tend to infinity. It is also observed, see Fig. 2b, that the values of $\Delta \sigma_{\ell}/\mu$ for both solutions are very close and their magnitudes become very large when β is approaching β_1 and β_2 .

7. Numerical results

We reiterate that all the results of this section are obtained using 800 Gaussian points to assure the accuracy of integration, as explained in Section 5.2.3. Also, the values of the kernels of all regular integrals involved in Eq. (42) are evaluated using Taylor series expansions when $|\bar{\beta} - \bar{\beta}_0| \leq 0.1$, in order to avoid near singularity. As in Mogilevskaya et al. (2021b), we adopted the intervals for the parameters $\tilde{\sigma}_0$ and γ to be $\tilde{\sigma}_0 \in [10^{-4}, 10^{-1}]$, $\gamma \in [10^{-1}, 10^3]$.

7.1. Convergence analysis

Consider the following arcs: (i) short arc ($\beta_1 = 89\pi/180$, $\beta_2 = 91\pi/180$), (ii) medium arc ($\beta_1 = \pi/4$, $\beta_2 = 3\pi/4$), and (iii) long arc ($\beta_1 = 0$, $\beta_2 = \pi$), all with the radius R = 1. Assume that $\sigma_0 = 0$, in which case Eq. (37) and Eq. (38) are fully decoupled, $\tilde{\sigma}^S$ can be

21

evaluated independently from ω^S , and the elastic fields outside of the arcs and across them can be expressed via $\tilde{\sigma}^S$ only. The rest of the parameters are set as $\tilde{\sigma}_{22}^{\infty}=1$, $\tilde{\sigma}_{11}^{\infty}=\tilde{\sigma}_{12}^{\infty}=0$, $\nu=0.33$, and $\gamma=0.1$. Convergence of the results for $\tilde{\sigma}^S$ for the three types of arcs with the increase in value of the truncation parameter m is demonstrated on Fig. 3. It can be concluded that, for the chosen value of γ , the results converge at m=40.

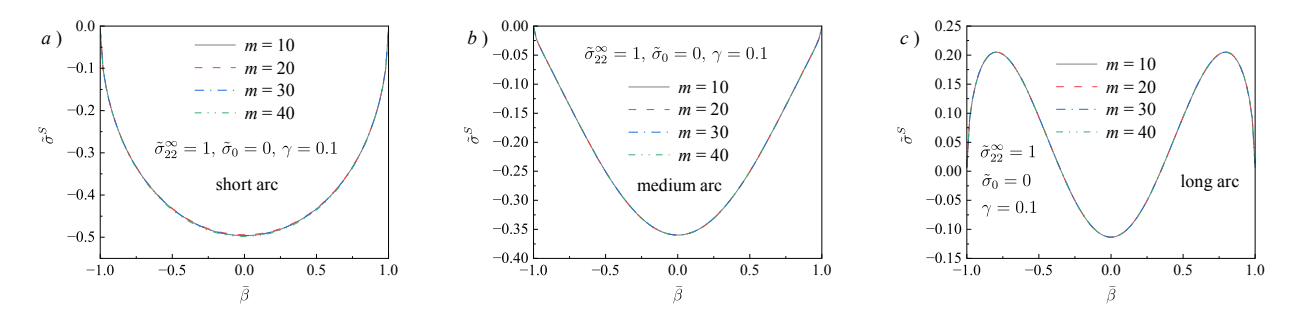


Figure 3: Values of $\tilde{\sigma}^S$ as functions of m for the three types of arcs.

We also investigated the convergence of the results for the dimensionless traction jumps $\Delta \tilde{\sigma} = \Delta \sigma / \mu = \Delta \tilde{\sigma}_n + i \Delta \tilde{\sigma}_\ell$ obtained via $\tilde{\sigma}^S$ using Eqs. (55). From the latter equations it can be seen that $\Delta \tilde{\sigma}_n$ is a linear function of $\tilde{\sigma}^S$ and, therefore, on Fig. 4 we plot the corresponding results for $\Delta \tilde{\sigma}_\ell$ only.

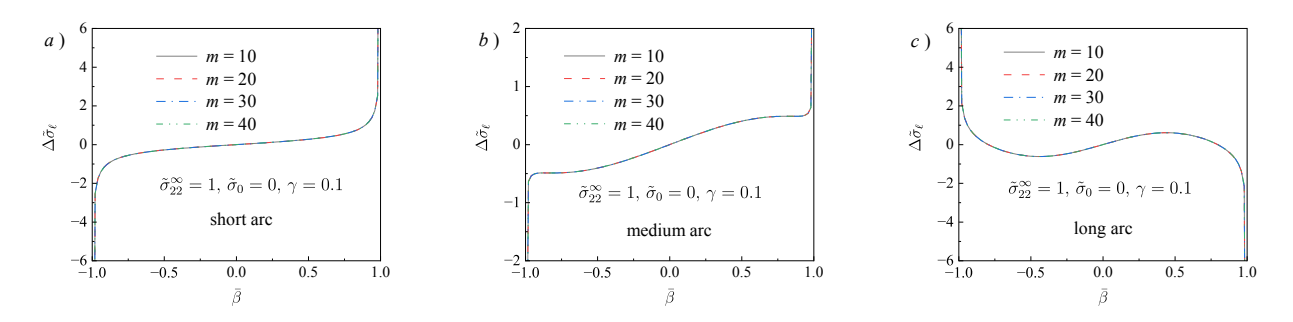


Figure 4: Values of $\Delta \tilde{\sigma}_{\ell}$ as functions of m for the three types of arcs.

From Fig. 4, it can also be seen that, for the chosen value of γ , the results converge at m = 40. We will use this number in numerical simulations below for the cases of small

to medium values of γ . However, as in the case of the straight segment considered in Mogilevskaya et al. (2021b), accurate solutions for the cases of $\gamma \geq 10^2$ would require the use of larger truncation numbers. We will discuss this issue in Section 7.2.2.

7.2. Parametric study

7.2.1. Influence of arc length θ

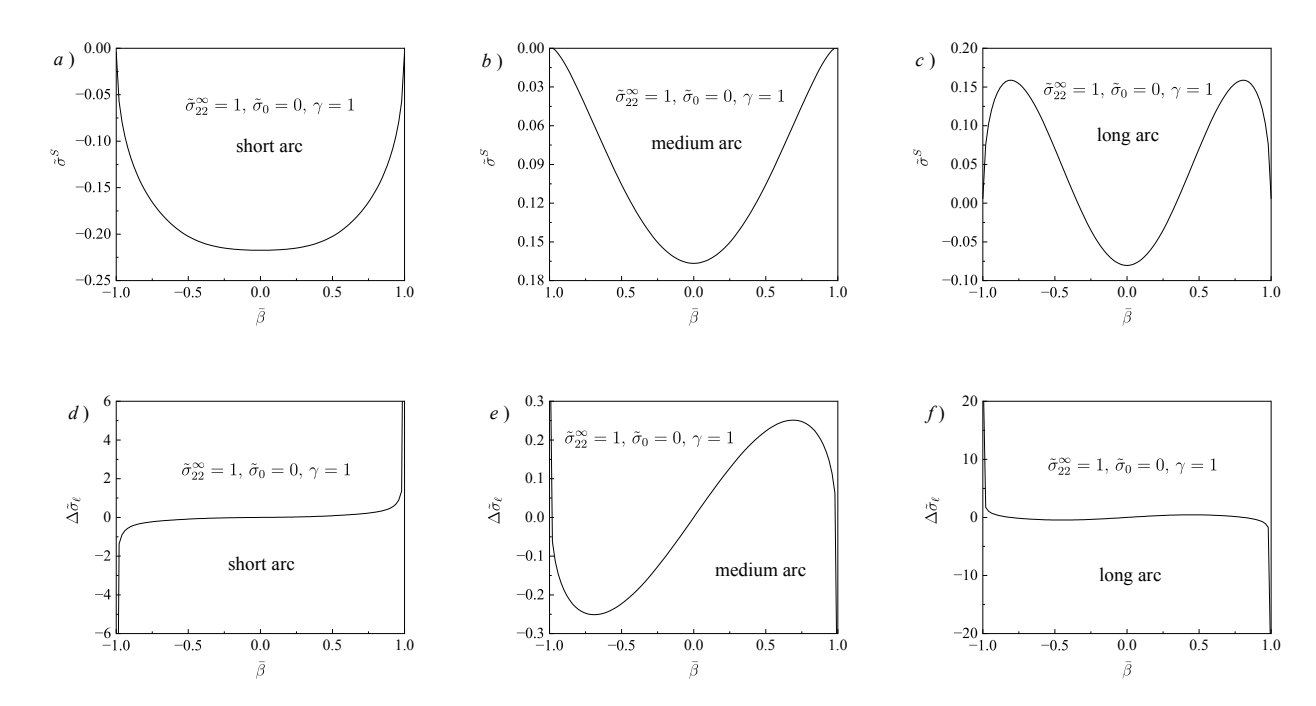


Figure 5: Distributions of $\tilde{\sigma}^S$ and $\Delta \tilde{\sigma}_{\ell}$ along the arcs.

As in Section 7.1, we consider the three types of arcs and assume the same values for the remaining parameters, except for γ that is now taken to be $\gamma=1$. The plots of Fig. 5 illustrate the distributions of $\tilde{\sigma}^S$ and $\Delta \tilde{\sigma}_\ell$ along the arcs. It can be seen that the values of $\tilde{\sigma}^S$ for arcs (i) and (ii) are negative. The interval of variations of $\tilde{\sigma}^S$ decreases from roughly $-0.25 < \bar{\beta} < 0$ for arc (i) to $-0.18 < \bar{\beta} < 0$ for arc (ii) and, in each case, there exists a single minimum at $\bar{\beta}=0$. The corresponding results for arc (iii) are located within a wider interval that includes both negative and positive values. In addition, the plot of $\tilde{\sigma}^S$ has three local extremes: maximum values of $\tilde{\sigma}^S=0.159$ are reached at $\bar{\beta}=\pm 0.8$ and its minimum

value of $\tilde{\sigma}^S = -0.0804$ is reached at $\bar{\beta} = 0$. The influence of arc length on $\Delta \tilde{\sigma}_{\ell}$ is even more dramatic, as can be seen from the same figure. The interval of variation of $\Delta \tilde{\sigma}_{\ell}$ first decreases as the arc length increases from case (i) to case (ii) but then significantly increases for case (iii); the behavior of the plot for case (iii) is completely reversed as compared to that for case (i). We can, therefore, conclude that the arc length has a profound effect on the problem's solutions. We have also compared the plots on Fig. 5 with those shown on Figs. 3 and 4 and concluded that with the increase in γ , the absolute values of $\tilde{\sigma}^S$ and $\Delta \tilde{\sigma}_{\ell}$ decrease, while the analysis of their behavior reveal the same trends when arc length increases, i.e. it can be seen from Fig. 3c, that, for a long arc, there also exist two maximum values $\tilde{\sigma}^S = 0.205$ reached at $\bar{\beta} = \pm 0.8$ and one minimum value $\tilde{\sigma}^S = -0.113$ reached at $\bar{\beta} = 0$.

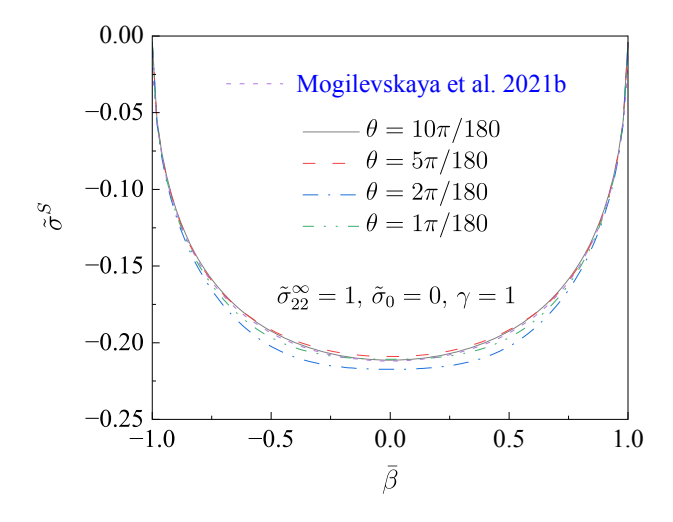


Figure 6: Distribution of $\tilde{\sigma}^S$ along short arcs vs that for a straight line.

It is interesting to compare our results with the results for the straight segment case shown on Fig. 5 of Mogilevskaya et al. (2021b), which were obtained here with the same parameters as in the latter paper. To do that, we set the arcs lengths to be $\theta = 10\pi/180$, $5\pi/180$, $2\pi/180$, $1\pi/180$ and plot the obtained results for $\tilde{\sigma}^S$ on Fig. 6. From that figure, it can be seen that the overall behavior of $\tilde{\sigma}^S$ does not change significantly in case of chosen values for θ and is somewhat similar to that for the straight segment case.

24

7.2.2. Influence of γ

We have already compared the results obtained with two values of γ for the case of arcs of various lengths. Here we perform more detailed comparison for the case of short arc (i).

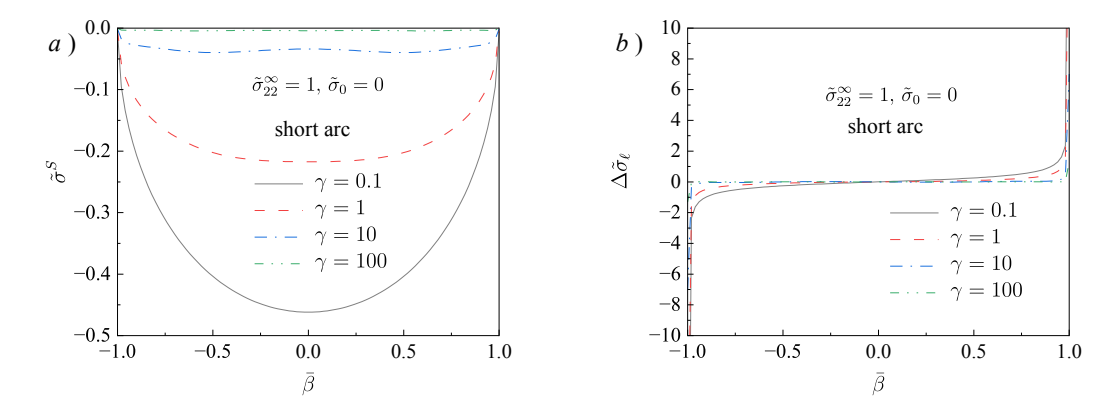


Figure 7: Distributions of $\tilde{\sigma}^S$ and $\Delta \tilde{\sigma}_{\ell}$ along the arc as functions of γ .

To do that, we adopt the same values for the parameters R, $\tilde{\sigma}_{ij}^{\infty}$, ν , and $\tilde{\sigma}_0$ as in the previous examples, while considering four different values of γ , i.e. $\gamma = 0.1$, 1, 10, 100. The corresponding results for $\tilde{\sigma}^S$ and $\Delta \tilde{\sigma}_{\ell}$ obtained with our solutions are plotted on Fig. 7. The results for $\tilde{\sigma}^S$ for $\gamma \geq 100$ exhibited oscillations, due to the Gibbs phenomenon near the tips. Similarly as in Mogilevskaya et al. (2021b), see the results of Fig. 5 of that paper, higher order truncation number up to m = 125 as well as spectral filter procedure in Sarra (2006) are required to obtain smoother solutions.

From Fig. 7a we can conclude that with the increase in γ , the value of $\tilde{\sigma}^S$ tends to 0, as it should, because according Eq. (37) $\tilde{\sigma}^S \to \tilde{\sigma}_0$ as $\gamma \to \infty$ and we took $\tilde{\sigma}_0=0$. With the decrease in γ , the interval of variation of $\tilde{\sigma}^S$ significantly increases and, for small γ , a single minimum is reached at $\bar{\beta}=0$, as it can be clearly seen for the case of $\gamma=0.1$. The changes in behavior of $\Delta \tilde{\sigma}_\ell$ with the increase in γ , shown on Fig. 7b, are mostly happening near the tips. This can be explained by the fact that $\Delta \tilde{\sigma}_\ell$ is proportional to the derivative $\tilde{\sigma}^S$ where the value of $\tilde{\sigma}^S$ changes abruptly.

25

7.2.3. Influences of surface tension $\tilde{\sigma}_0$

Consider the case of arc (ii), assume that $\gamma = 1$, $\tilde{\sigma}_{22}^{\infty} = 1$, R = 1, $\nu = 0.33$, and take the following values of $\tilde{\sigma}_0 = 0.01$, 0.05, 0.1. In this case, $\tilde{\sigma}_0 \neq 0$ and, therefore, the system of Eqs. (37), (38) cannot be decoupled. The values of $\tilde{\sigma}^S$ and ω^S obtained from that equations are plotted on Fig. 8.

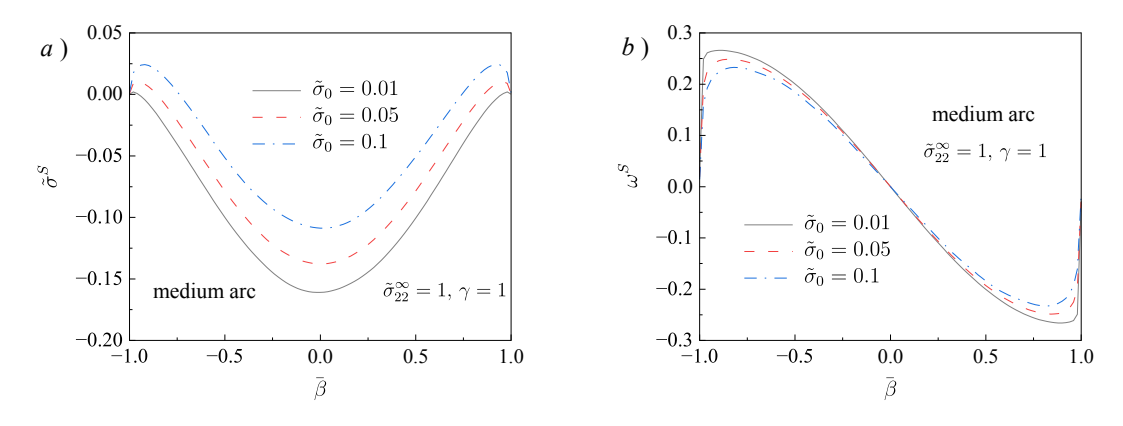


Figure 8: Distributions of $\tilde{\sigma}^S$ and ω^S along the arc as functions of $\tilde{\sigma}_0$.

From Fig. 8a we can see that the plots of $\tilde{\sigma}^S$ exhibit similar behavior with Fig. 5b, but the absolute values of surface stress decrease with the increase of surface tension $\tilde{\sigma}_0$. The same is true for the plots of and ω^S . Due to symmetry of the geometry and remote load, $\tilde{\sigma}^S$ is symmetric in respect to y-axis, while ω^S is anti-symmetric.

Since $\sigma_0 \neq 0$, the values of $\Delta \tilde{\sigma}_n$ and $\Delta \tilde{\sigma}_\ell$ are computed from Eqs. 2, 3 using both $\tilde{\sigma}^S$ and ω^S . These values are plotted on Fig. 9. Due to fast change in values of $\tilde{\sigma}^S$ and ω^S near the tips, the values of $\Delta \tilde{\sigma}_n$ and $\Delta \tilde{\sigma}_\ell$ become very large there, while the corresponding values outside of the tips vicinities vary less.

7.2.4. Modeling of local fields in composites reinforced with graphene-oxide membranes

For illustration purposes, we consider epoxy matrix with $\mu = 2$ GPa, $\nu = 0.35$ containing the arc characterized by R = 5 nm and $\beta_1 = \pi/4$, $\beta_2 = 3\pi/4$. The two-dimensional elastic

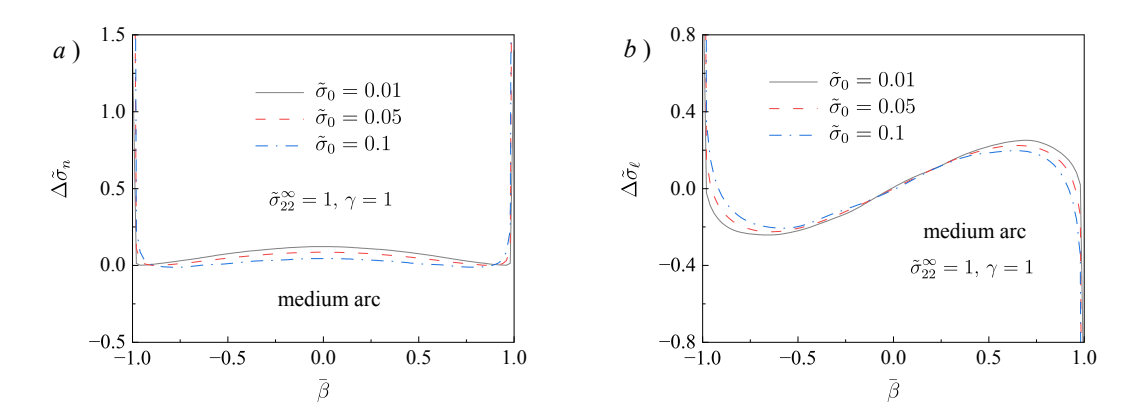


Figure 9: Distributions of $\Delta \tilde{\sigma}_n$ and $\Delta \tilde{\sigma}_\ell$ along the arc as functions of $\tilde{\sigma}_0$.

properties of the arc are chosen to be equal to those reported in Suk et al. (2010), which results in the following dimensionless parameters: $\gamma = 0.12$ and $\tilde{\sigma}_0 = 0.025$.

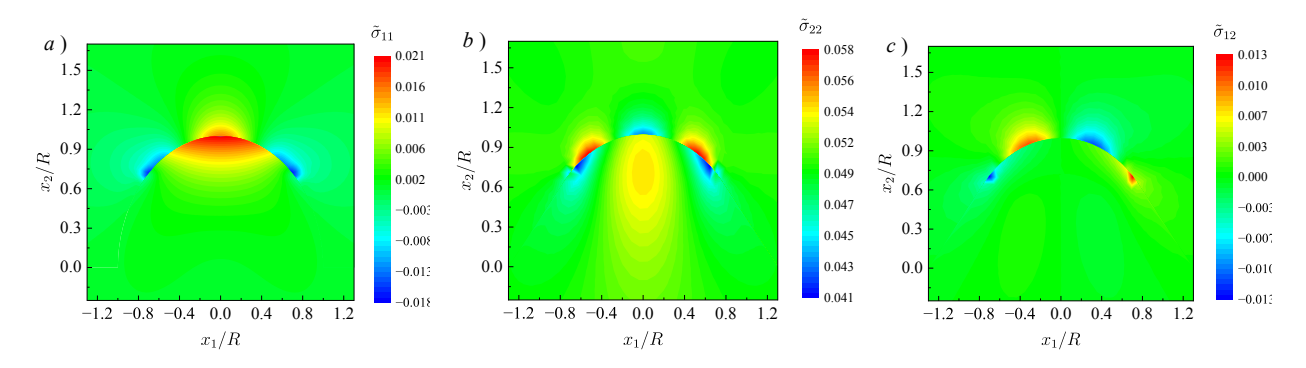


Figure 10: Dimensionless Cauchy stresses for the case of remote loading $\tilde{\sigma}_{22}^{\infty} = 0.05$.

We first assume that the only non-zero component of the far-field is $\sigma_{22}^{\infty} = 100$ MPa Mogilevskaya et al. (2008), which is $\tilde{\sigma}_{22}^{\infty} = \sigma_{22}^{\infty}/\mu = 0.05$. The dimensionless Cauchy stresses $\tilde{\sigma}_{ij}$ in the domain $x_1 \otimes x_2 \in [-6.5, 6.5] \otimes [-1.25, 8.5]$ (nm) are plotted on Fig. 10. It can be seen from Fig. 10a and b that while the distributions of $\tilde{\sigma}_{11}$ and $\tilde{\sigma}_{22}$ are symmetric with respect to x_2 -axis, the distribution $\tilde{\sigma}_{12}$ is anti-symmetric as in Fig. 10c. The mechanical properties in this example are the same as those used in Mogilevskaya et al. (2021b), where L was assumed to be a straight segment and far-field load was of the same type (but of

different magnitude). Comparison of our results with the corresponding contour plots of Fig. 11 in Mogilevskaya et al. (2021b), shows that the curvature-induced effects manifest themself in lack of symmetry of stress fields with respect to x_1 -axis, which is expected. Also, it can be clearly seen that all components $\tilde{\sigma}_{ij}$ in Fig. 10 undergo jumps across the arc.

From Fig. 10a, it can be observed that $\tilde{\sigma}_{11}$ are tensile inside of the most of the region, which demonstrates that the effect of Poisson's ratio in the bulk (under the vertical far-filed $\tilde{\sigma}_{22}^{\infty} = 0.05$) is less than that of positive surface tension $\tilde{\sigma}_0$. Near the tips $\tilde{\sigma}_{11}$ is compressive and exhibits singular behavior, while the tensile stresses are concentrated right under the arc. From Fig. 10b, it can be concluded that $\tilde{\sigma}_{22}$ is tensile everywhere in the region of interest. It is seen from Fig. 10c that $\tilde{\sigma}_{12}$ along the arc is anti-symmetric and exhibit singular behavior near the tips.

We then consider the same example but take the remote load to be $\tilde{\sigma}_{11}^{\infty} = 0.05$. The mechanical properties and geometries are the same with the previous example. Dimensionless Cauchy stresses $\tilde{\sigma}_{ij}$ in the same region are plotted on Fig. 11, from which we can conclude that the resulting $\tilde{\sigma}_{11}$ and $\tilde{\sigma}_{22}$ are symmetric to x_2 -axis, while $\tilde{\sigma}_{12}$ is anti-symmetric.

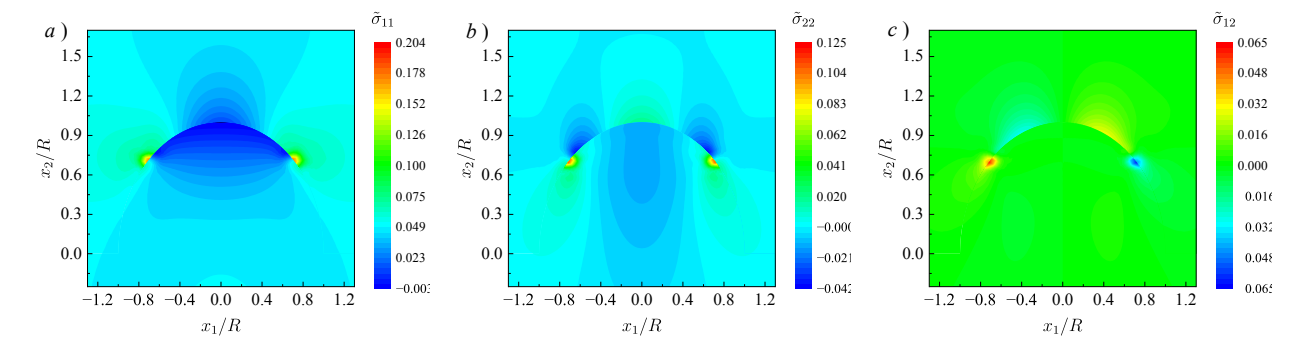


Figure 11: Dimensionless Cauchy stresses for the case of remote loading $\tilde{\sigma}_{11}^{\infty} = 0.05$.

From Fig. 11a, it is found that $\tilde{\sigma}_{11}$ is tensile inside the most of the region. However, it is interesting to note that $\tilde{\sigma}_{11}$ is compressive right under the arc, which illustrates an important role of the curvature and surface tension. From Fig. 11b, we observe that stress

8 CONCLUSIONS 28

 $\tilde{\sigma}_{22}$ is mostly tensile, which, again, indicates that the effect of the Poisson ratio in the bulk is less than that of positive surface tension. The values of $\tilde{\sigma}_{22}$ are negative in close vicinities of the tips. Fig. 11c indicate again that $\tilde{\sigma}_{12}$ is anti-symmetric.

We finally consider the remote shear load $\tilde{\sigma}_{12}^{\infty} = 0.05$. The mechanical properties and geometries are again the same as in the previous examples. Dimensionless Cauchy stresses $\tilde{\sigma}_{ij}$ inside the same region are plotted on Fig. 12.

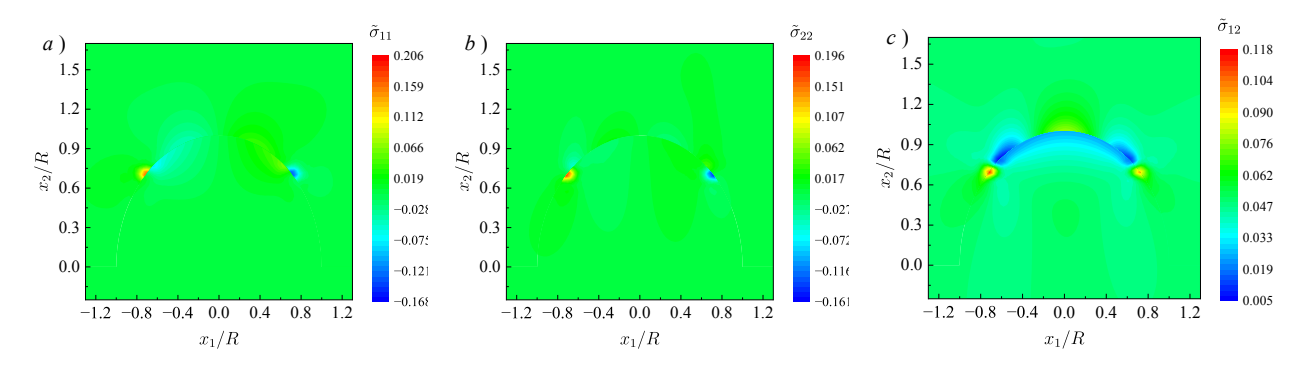


Figure 12: Dimensionless Cauchy stress fields or the case of remote loading $\tilde{\sigma}_{12}^{\infty} = 0.05$.

From Fig. 12 we can conclude that under remote shear load $\tilde{\sigma}_{12}$, $\tilde{\sigma}_{11}$ and $\tilde{\sigma}_{22}$ are antisymmetric, while $\tilde{\sigma}_{12}$ is symmetric due to the symmetry of remote load and geometry. In this case, the traction jumps are not as pronounced as ones shown on Fig. 10 and Fig. 11. We could still observe singular behavior of the stresses near the tips.

8. Conclusions

In this paper, we solved for the first time the plane strain problem of an infinite isotropic elastic matrix subjected to uniform far-field load and containing a Gurtin-Murdoch material surface of cylindrical shape. The solution allows for accurate evaluations of all elastic fields everywhere in the material system. The analysis of the analytical and numerical results, obtained in the paper, lead to the following important conclusions. First, we demonstrated that, unlike for the straight segment case considered in Mogilevskaya et al. (2021b), the

8 CONCLUSIONS 29

equations for the components of the surface stress tensor are always coupled, when the surface tension is present. Second, we found out that, unlike for the straight segment case, the problem under study is never reducible to that of a rigid arc. This fact can be explained using the Benveniste and Miloh classification of thin interphase layers in which the Gurtin-Murdoch jump conditions and those for a rigid arc describe two distinct interface regimes. Third, we demonstrated that, even for the case of zero surface tension, the arc length has a profound influence on the distribution of surface stress, which represents one of the curvature-induced effects. We also investigated the influence of the remaining dimensionless parameters with the focus on curvature-induced effects.

The obtained solution has important theoretical and practical applications. From the theoretical standpoint it can be used as a benchmark example for the numerical solutions of the problems involving membranes of arbitrary sufficiently smooth shapes, that is a subject of our future work. We plan to modify the present approach in order to use the more complete Steigmann-Ogden theory that includes bending effects of the material surface. The methods developed here will be helpful for solving more complex three-dimensional problems that are also a subject of our future work. On a practical side, the solution could be used for modeling mechanical processes in composite materials reinforced by ultra thin prestressed stiff flexible membranes.

Acknowledgments

Zhilin Han gratefully acknowledges support from the National Natural Science Foundation of China through NSFC No. 12002084 and the support from Shanghai High Performance Fibers and Composites Center (Province-Ministry Joint), Center for Civil Aviation Composites, Donghua University. Sofia G. Mogilevskaya gratefully acknowledges the support from the National Science Foundation, United States, award number NSF CMMI-2112894. Anna Y. Zemlyanova gratefully acknowledges the support from the Simons Collaboration

REFERENCES 30

Grant for Mathematicians (2020-2025), award number 713080.

References

- Baranova, S., Mogilevskaya, S., Mantic, V., and Jiménez-Alfaro, S. (2020). Analysis of the antiplane problem with an embedded zero thickness layer described by the Gurtin-Murdoch model. *J. Elast.*, 140:171–195.
- Benveniste, Y. and Miloh, T. (2001). Imperfect soft and stiff interfaces in two-dimensional elasticity. *Mech. Mater.*, 33:309–323. 6
- Cao, G. (2014). Atomistic studies of mechanical properties of graphene. Polymers, 6:2404–2432. 1
- Güler, O. and Bağcı, N. (2020). A short review on mechanical properties of graphene reinforced metal matrix composites. J. Mater. Res. Technol., 9:6808–6833. 1
- Gurtin, M. and Murdoch, A. (1975). A continuum theory of elastic material surfaces. *Arch. Ration. Mech. Anal.*, 57:291–323. 1
- Gurtin, M. and Murdoch, A. (1978). Surface stress in solids. Int. J. Solids Struct., 14:431-440. 1
- Lin'kov, A. and Mogilevskaya, S. (1990). Hypersingular integrals in plane problems of the theory of elasticity. *PMM-J. Appl. Math. Mech.*, 54(1):93–99. 5.2.2
- Linkov, A. and Mogilevskaya, S. (1998). Complex hypersingular BEM in plane elasticity problems. In: Sladek, V., Sladek, J. (Eds.), Singular Integrals in Boundary Element Method, Chapter 9. Computational Mechanics Publication, pages 299–364. 3.2
- Liu, Y. and Jiang, C. (1994). Stress distribution at the rigid circular arc inclusion end. *Eng. Fract. Mech.*, 47(3):431–440. 1, 6, 6, 6, 6, 2, 6
- Martin, P. (1992). Exact solution of a simple hypersingular integral equation. J. Integral Equ. Appl., pages 197–204. 5.2.2, 5.2.2, 5.2.2
- Mirzaei, M. and Abbasi, M. (2023). Dynamic response of moderately thick graphene reinforced composite cylindrical panels under the action of moving load. *Eng. Anal. Bound. Elem.*, 146:292–305. 1
- Mogilevskaya, S., Crouch, S., and Stolarski, H. (2008). Multiple interacting circular nano-inhomogeneities with surface/interface effects. J. Mech. Phys. Solids, 56:2928–2327. 7.2.4
- Mogilevskaya, S. and Linkov, A. (1998). Complex fundamental solutions and complex variables boundary element method in elasticity. *Comput. Mech.*, 22:88–92. 3.2
- Mogilevskaya, S., Zemlyanova, A., and Kushch, V. (2021a). Fiber- and particle-reinforced composite ma-

REFERENCES 31

terials with the Gurtin–Murdoch and Steigmann–Ogden surface energy endowed interfaces. Appl. Mech. Rev., 73(5). 2, 3.1, 3.1, 3.2

- Mogilevskaya, S., Zemlyanova, A., and Mantič, V. (2021b). The use of the Gurtin-Murdoch theory for modeling mechanical processes in composites with two-dimensional reinforcements. *Compos. Sci. Technol.*, 210:108751. 1, 2, 3.1, 3.2, 3.2, 3.3, 5.1, 6, 7, 7.1, 7.2.1, 7.2.2, 7.2.4, 8
- Papageorgiou, D., Kinloch, I., and Young, R. (2017). Mechanical properties of graphene and graphene-based nanocomposites. *Prog. Mater. Sci.*, 90:75–127. 1
- Papageorgiou, D., Li, Z., Liu, M., Kinloch, I., and Young, R. (2020). Mechanisms of mechanical reinforcement by graphene and carbon nanotubes in polymer nanocomposites. *Nanoscale*, 12:2228–2267. 1
- Sarra, S. (2006). Digital total variation filtering as postprocessing for chebyshev pseudospectral methods for conservation laws. *Numer. Algorithms*, 41:17–33. 7.2.2
- Steigmann, D. and Ogden, R. (1997). Plain deformations of elastic solids with intrinsic boundary elasticity.

 Proc. R. Soc. London A, 453:853–877. 1
- Steigmann, D. and Ogden, R. (1999). Elastic surface-substrate interactions. Proceedings of the Royal Society of London. Series A: Mathematical, Physical and Engineering Sciences, 455(1982):437–474. 1
- Suk, J., Piner, R., An, J., and Ruoff, R. (2010). Mechanical properties of monolayer graphene oxide. ACS Nano, 4:6557–6564. 1, 7.2.4
- Zemlyanova, A. Y., Mogilevskaya, S. G., and Schillinger, D. (2023). Numerical solution of the two-dimensional steigmann–ogden model of material surface with a boundary. *Physica D*, 443(133531). 1, 2, 3.1, 3.2, 3.2, 3.3, 5.1